

Radiation Budget of the Tropical Intraseasonal Oscillation

JIA-LIN LIN AND BRIAN E. MAPES

NOAA-CIRES Climate Diagnostics Center, Boulder, Colorado

(Manuscript received 13 August 2003, in final form 14 December 2003)

ABSTRACT

This study examines the relationship between precipitation and radiative heating on intraseasonal time scales in the Tropics using collocated top-of-atmosphere (TOA) and surface radiative flux measurements from special field program data [Atmospheric Radiation Measurement (ARM) Program and Tropical Ocean Global Atmosphere Coupled Ocean-Atmosphere Response Experiment (TOGA COARE) experiments] as well as long-term TOA flux data [from Earth Radiation Budget Experiment (ERBE) and Advanced Very High Resolution Radiometer (AVHRR) satellite data]. All the different datasets consistently show that the atmosphere-integrated radiative heating is nearly in phase with the precipitation and enhances the net condensation heating by about 10%–15%. The dominant contribution to this radiative warming during wet periods is the reduction of TOA outgoing longwave radiation (OLR), primarily by clouds but with a small contribution by water vapor. This radiative heating is reduced slightly by enhanced surface downwelling longwave radiation, attributable to low cloud bases and reduced atmospheric shortwave absorption attributable to shadowing by high cloud tops.

The intraseasonal budget of TOA radiation, reflecting heating of the whole ocean plus atmosphere column, is characterized by shortwave cloud forcing anomalies that are substantially larger than the longwave cloud forcing anomaly. This imbalance is in contrast with the near cancellation between these two terms at the seasonal time scale.

1. Introduction

The tropical intraseasonal oscillation (ISO), discovered by Madden and Julian (1971, 1972), is an important mode of tropical convection and circulation (e.g., Weickmann et al. 1985; Lau and Chan 1985; Salby and Hendon 1994; Wheeler and Kiladis 1999). It affects a wide range of tropical and extratropical weather (e.g., Yasunari 1979; Hendon and Liebmann 1990; Liebmann et al. 1994; Higgins and Mo 1997) and the onset and decay of some of the El Niño events (e.g., Kessler et al. 1995; Takayabu et al. 1999; Bergman et al. 2001). Therefore, the ISO is important for both extended-range weather forecasting and long-term climate prediction.

Tropical intraseasonal variability is poorly simulated in general circulation models (GCMs). Typically, simulated phenomena are too weak and propagate too fast (e.g., Hayashi and Sumi 1986; Hayashi and Golder 1986, 1988; Lau et al. 1988; Slingo et al. 1996). It is our hope that observational studies of major budget terms may offer useful guidance on how to improve ISO simulations and forecasts in models.

Diabatic heating is crucial to the ISO in the Eastern Hemisphere (Krishnamurti et al. 1985; Murakami and

Nakazawa 1985; Yanai et al. 2000). The heating is strongly associated with a propagating large-scale circulation anomaly (e.g., Madden and Julian 1972; Weickmann et al. 1985; Salby and Hendon 1994), and this propagating circulation anomaly (hereafter called a wave) also feeds back onto the heating (Hendon and Salby 1994; Zhang 1996), suggesting a wave-heating feedback theoretical framework for the ISO. The total diabatic heating has two main components: convective heating (release of latent heat, along with eddy flux divergences that shape the profile) and radiative heating. Most theoretical studies have focused only on the role of convective heating in wave-heating feedback. The mechanisms studied include the wave-CISK (conditional instability of the second kind) mechanism (e.g., Lau and Peng 1987), the wind-induced surface heat exchange (WISHE) mechanism (e.g., Emanuel 1987; Neelin et al. 1987), and the charge-discharge mechanism (e.g., Blade and Hartmann 1993; Hayashi and Golder 1997).

Recently, several modeling studies found that radiative heating can also significantly affect the amplitude and/or phase speed of the simulated intraseasonal oscillations (Raymond 2001; Lee et al. 2001; Sobel and Gildor 2003). In the convectively active phase of the ISO, clouds and water vapor associated with deep convection reduce outgoing longwave radiation (OLR) to space and therefore increase radiative heating in the

Corresponding author address: Dr. Jia-Lin Lin, NOAA-CIRES Climate Diagnostics Center, 325 Broadway, R/CDC1, Boulder, CO 80305.
E-mail: jialin.lin@noaa.gov

atmosphere, which tends to reinforce the preexisting convective heating. As a quantitative measure, an *enhancement factor of radiative heating* can be defined as the ratio between the column-integrated radiative heating and the column-integrated convective heating. In an idealized model of thermodynamic atmosphere–ocean interaction on the intraseasonal time scale, Sobel and Gildor (2003) found that the enhancement factor of radiative heating is the most sensitive parameter, and both the growth rate and the period of simulated intraseasonal oscillations increase with the enhancement factor. In a set of atmospheric GCM simulations of the ISO, Lee et al. (2001) found that the amplitude, phase speed, and even direction of propagation of intraseasonal variability are very sensitive to the enhancement factor of radiative heating, which can be varied, for example, by changing cloud microphysical assumptions. In a theoretical model, Raymond (2001) demonstrated that when the enhancement factor is very large the radiative heating can reduce the effective static stability to a negative value, that is, to an effective static instability. He termed this instability the *radiative–convective instability*. An ISO-like slow eastward-propagating mode appears to develop in his model from this radiative–convective instability. In order to reach such radiative–convective instability, the enhancement factor of radiative heating may need to be larger than 20%, as estimated by Lee et al. (2001) based on the vertical structure assumptions of Yu et al. (1998).

The high sensitivity of the preceding ISO models to the enhancement factor of radiative heating raises the following questions for observation. What is the observed value of enhancement factor in the ISO? Does it reach the critical value of 20% for radiative–convective instability? Is the radiative heating well in phase with the convective heating, or is there a phase lag between them? Apart from the OLR, do other terms (such as surface downwelling longwave flux or atmospheric shortwave absorption) also contribute importantly to the anomalous radiative heating?

Most previous observational studies of the earth's radiation budget using satellite data focused on climatological mean patterns and seasonal-to-interannual variations (e.g., Vonder Haar and Suomi 1969; Cess 1976; Ramanathan et al. 1989; Harrison et al. 1990; Cess et al. 2001). Most previous observational studies of the atmospheric radiation budget using collocated satellite–surface data also focused on climatological mean values (e.g., Cess et al. 1995, 1996; Collins et al. 1996; Chou et al. 1998). Few studies have been done on the time-varying radiation budget associated with perturbations around the seasonal mean. Johnson and Ciesielski (2000) derive indirectly the column-integrated radiative heating from the sounding array budget during Tropical Ocean Global Atmosphere Coupled Ocean–Atmosphere Response Experiment (TOGA COARE) and found a very strong intraseasonal variation. However, after the humidity bias in the original sounding data was cor-

rected, they recalculated the column-integrated radiative heating and found a much smaller intraseasonal variation (Ciesielski et al. 2002; see Fig. 8b below). Therefore, it is still unclear how much the column-integrated radiative heating enhances the column-integrated convective heating in the ISO.

In this study, we derive intraseasonal variations in the radiation budget directly from collocated top-of-atmosphere (TOA) and surface radiative flux measurements. Atmospheric Radiation Measurement (ARM) Program and TOGA COARE experiments provide intensive special datasets, while long-term TOA flux measurements from the Earth Radiation Budget Experiment (ERBE) and Advanced Very High Resolution Radiometer (AVHRR) offer larger statistical samples. Indirect budget-residual estimates from COARE are also compared.

The datasets used in this study are described in section 2. The time filtering and intraseasonal composite (regression) methods are described in section 3. The radiation budget results are reported in section 4, divided into atmospheric (section 4a), TOA (section 4b), and surface (section 4c). A summary is given in section 5.

2. Data

The datasets used in this study are summarized in Table 1. The radiation datasets used include collocated TOA and surface radiative fluxes from ARM and TOGA COARE, column-integrated radiative heating derived indirectly from TOGA COARE sounding array budgets, and long-term TOA fluxes from ERBE and AVHRR. For comparison with column-integrated convective heating, corresponding precipitation data have also been used. To bracket the uncertainties associated with precipitation measurements/estimates, multiple precipitation datasets are used when available. The following subsections detail the datasets from ARM (2a) and COARE (2b), with point-sampling issues considered in section 2c. Section 2d summarizes the long-term ERBE and AVHRR satellite datasets.

a. Collocated TOA and surface fluxes for ARM

The collocated TOA and surface fluxes for the ARM tropical western Pacific (TWP) Manus site (Fig. 3a) include TOA fluxes from Geostationary Meteorological Satellite (GMS; Minnis et al. 1995; Doelling et al. 1998) and surface downwelling fluxes from Clouds and Earth's Radiant Energy System (CERES) ARM Validation Experiment (CAVE; Rutan et al. 2001), which covers a 14-month period from April 2000 to May 2001. The Manus site is located at 2°S, 147°E with an elevation of 6 m.

The GMS TOA fluxes (Minnis et al. 1995; Doelling et al. 1998) include broadband shortwave (SW) albedo and longwave (LW) flux, which are converted from the GMS narrowband measurements using narrowband–broadband relationships derived from historical collo-

TABLE 1. Datasets used in this study.

Project	Variables	Instrument	Reference
Collocated data for ARM Manus site (Apr 2000–May 2001)	TOA fluxes	GMS CERES	Minnis et al. (1995) Wielicki et al. (1996)
	Surface fluxes	ARCS	Mather et al. (1998)
	Precipitation	CMAP	Xie and Arkin (1997)
	Clouds	GMS	Minnis et al. (1995)
	Atmosphere T, q	Sounding	
Collocated data for TOGA COARE (Nov 1992–Feb 1993)	TOA fluxes	GMS	Minnis et al. (1995)
	Surface fluxes	Five-station avg	Kreuger and Burks (1998)
	Precipitation	SSM/I VIS–IR MSU	Curry et al. (1999) Spencer (1993)
	Clouds	Budget ISCCP	Ciesielski et al. (2002) Rossow and Garder (1993)
	Atmosphere T, q	Sounding	
Long-term data	TOA fluxes	ERBE AVHRR	Barkstrom and Smith (1986) Liebmann and Smith (1996)
	Precipitation	CMAP	Xie and Arkin (1997)
		GPI	Janowiak and Arkin (1991)
		MSU	Spencer (1993)

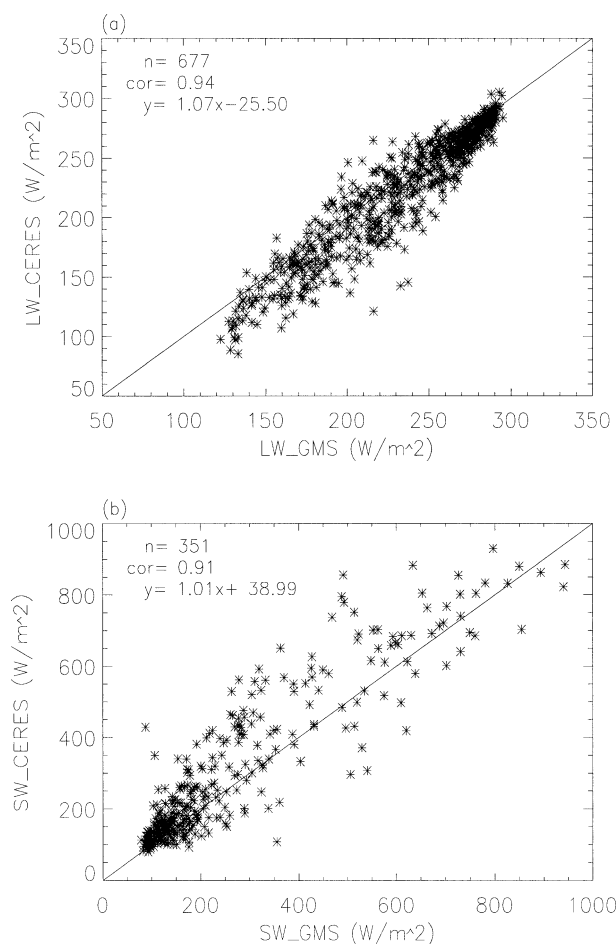


FIG. 1. Scatter diagram of CERES vs GMS hourly TOA (a) LW flux and (b) SW flux over a $30 \text{ km} \times 30 \text{ km}$ area surrounding Manus Island for 13 months from Apr 2000 to May 2001.

cated GMS and ERBE measurements. The data cover a $0.3^\circ \times 0.3^\circ$ area surrounding Manus Island with a temporal resolution of 1 h. The missing values are filled with linear interpolation in time allowing no more than two consecutive missing hours. The upwelling SW flux is then calculated from the albedo and the downward TOA SW flux (computed from the solar constant and solar zenith angle). The hourly data are averaged into daily data only when the number of missing hours is no more than two for the SW flux. Otherwise, the daily value is assigned missing. The daily data are then averaged to pentad data.

To validate the GMS TOA fluxes, we use the collocated CERES broadband measurements (Wielicki et al. 1996) stored in the CAVE archive. The CERES data are twice daily and do not sample a full diurnal cycle, so they could not be used directly. Figure 1 shows the comparison of hourly GMS fluxes with available CERES measurements within the same hour averaged over a $30 \text{ km} \times 30 \text{ km}$ area surrounding the Manus site. Both the GMS LW and SW fluxes correlate well with the corresponding CERES measurements. The LW flux has a small negative bias (7%). This bias, when reflected in the intraseasonal anomaly (see Fig. 10 below), is only $1\text{--}2 \text{ W m}^{-2}$, which would not affect our conclusions. The SW flux is not biased, although it is more scattered than the LW flux.

The GMS TOA fluxes have also clear-sky values, making it possible to calculate the cloud radiative forcing (CRF). The LW CRF at TOA is defined as

$$\text{LWCRF} = F_{\text{clr}} - F,$$

where F is the all-sky upwelling LW flux at TOA, and F_{clr} is the clear-sky upwelling LW flux at TOA. The SW CRF is defined as

$$\text{SWCRF} = R_{\text{clr}} - R,$$

where R is the all-sky upwelling (reflected) SW flux at TOA, and R_{clr} is the clear-sky upwelling SW flux at TOA.

The surface radiative fluxes were measured by the Atmospheric Radiation and Cloud Stations (ARCS; Mather et al. 1998). Variables used include downwelling global SW flux and shaded downwelling LW flux. The temporal resolution is 60 s. The ARCS surface fluxes are averaged to hourly data. There are a few missing values and they are filled using linear interpolation in time. The hourly data are then averaged to daily data, and the daily data are further averaged to pentad data. The surface upwelling SW flux is calculated from downwelling SW flux by taking the surface SW albedo as 0.055 following Weller and Anderson (1996) and Burks (1998). The surface upwelling LW flux is also calculated following Weller and Anderson (1996) using $LW_{\text{up}} = \epsilon_{\text{ss}} \sigma T_s^4 - (1 - \epsilon_{\text{ss}}) LW_{\text{dn}}$, where T_s is the sea surface temperature, σ is the Stefan–Boltzmann constant, and ϵ_{ss} is the longwave emissivity of the sea surface taken as 0.97. A graybody approximation is used so that the surface longwave albedo is equal to one minus the emissivity. The sea surface temperature comes from the National Oceanic and Atmospheric Administration (NOAA) Optimum Interpolation Sea Surface Temperature data (Reynolds et al. 2002).

The surface precipitation for ARM comes from Climate Prediction Center (CPC) Merged Precipitation Analysis (CMAP; Xie and Arkin 1997). The CMAP data are pentad data with a horizontal resolution of 2.5° latitude by 2.5° longitude. We average the four grids surrounding Manus Island.

Cloud information comes from GMS geostationary satellite data (Minnis et al. 1995; Doelling et al. 1998). In this study, we use the total cloud amount, averaged cloud-top height, and averaged cloud optical depth for the $0.3^\circ \times 0.3^\circ$ area surrounding Manus Island. Profiles of atmosphere temperature and water vapor mixing ratio come from the upper-air soundings at Manus Island.

b. Collocated TOA and surface fluxes for TOGA COARE

The collocated TOA and surface radiative fluxes averaged over the TOGA COARE Intensive Flux Array (IFA) area (Fig. 3a) were processed by Krueger and Burks (1998) and Burks (1998) for the 4-month period from November 1992 to February 1993. The TOA fluxes come from the GMS satellite data similar as above but processed for TOGA COARE (Minnis et al. 1995; Doelling et al. 1998). The surface fluxes are averages of measurements at five surface stations. The datasets are 3-hourly and are averaged to daily data.

We also use the column-integrated radiative heating derived indirectly from the TOGA COARE IFA sounding array budget by Ciesielski et al. (2002). The data are 6-hourly and are averaged to daily data.

The surface precipitation for TOGA COARE IFA

comes from three different estimates: the 3-hourly Special Sensor Microwave Imager (SSM/I) visible (VIS)–IR precipitation (Curry et al. 1999), the daily Microwave Sounding Unit (MSU) precipitation (Spencer 1993), and 6-hourly sounding array budget precipitation (Ciesielski et al. 2002). All the datasets are averaged to daily data.

The cloud information for TOGA COARE comes from the International Satellite Cloud Climatology Project (ISCCP; Rossow and Garder 1993). In this study, we use the total cloud amount, averaged cloud-top pressure, and averaged cloud optical depth. Profiles of atmosphere temperature and water vapor mixing ratio come from the upper-air soundings (Ciesielski et al. 2002).

c. Sampling issues for collocated TOA and surface measurements

A significant source of error in collocated satellite–surface measurements are sampling errors (Cess et al. 1996), which occur because the satellite pixel measurements are instantaneous and over a grid that is much larger than the field of view of an upward-facing pyranometer or pyrgeometer. A single isolated cloud could substantially impact the surface measurement while having little effect on the satellite measurement; the reverse would occur if there were clouds over most of the satellite grid but not over the surface instrument. Cloud systems move, however, so that, in a statistical context, temporally averaging the surface measurements can be equivalent to spatially averaging them over the satellite grid. This equivalence between temporal and spatial averaging has been demonstrated by Long and Ackerman (1995) and Cess et al. (1996) using collocated satellite–pyranometer measurements for a region in Wisconsin. Cess et al. (1996) show that 60-min temporal averaging at one station can represent well the spatial averaging over a network of stations covering a roughly $0.8^\circ \times 0.8^\circ$ grid. Long and Ackerman (1995) show that for any pair of stations the correlation between temporal averages at the two locations increases monotonically with averaging period, and reaches nearly 1 (perfect correlation) for daily average. In this study, all the collocated satellite–surface measurements are temporally averaged over a period longer than 1 day, and are further filtered using a 30–70-day bandpass filter (section 3). Therefore, the sampling error should be very small and would not affect our results in any substantial manner.

d. Long-term TOA fluxes from ERBE and AVHRR

The long-term datasets cover 5 yr from 1985 to 1989. They include the daily mean TOA fluxes from ERBE (Barkstrom and Smith 1986), the daily mean outgoing longwave radiation from NOAA AVHRR (Liebmann and Smith 1996), and three precipitation datasets: CMAP, Geostationary Operational Environmental Sat-

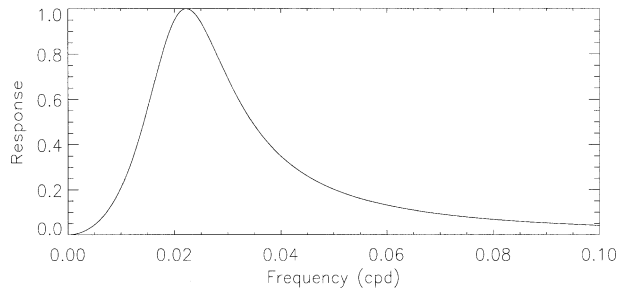


FIG. 2. The response function of the 30–70-day Murakami filter used in this study.

ellite (GOES) precipitation index (GPI; Janowiak and Arkin 1991), and Microwave Sounding Unit (MSU; Spencer 1993). All the long-term gridded datasets cover 5 yr from 1985 to 1989 except for the GPI precipitation, which starts from 1986. All the datasets have a horizontal resolution of 2.5° latitude by 2.5° longitude. We average the data to pentad data along the equator (between 5°N and 5°S) with a zonal resolution of 10° longitude.

3. Method

The ISO is a broadband phenomenon with an average period of 45 days and a spread from 20 to 80 days (see review by Madden and Julian 1994). To emphasize the broadband nature of the oscillation, previous studies used wide-frequency bands such as 30–60 days (Weickmann et al. 1985), 35–95 days (Salby and Hendon 1994), or 30–96 days (Wheeler and Kiladis 1999). In this study we also use a wide-frequency band of 30–70 days. All datasets are filtered using a 30–70-day Murakami (1979) filter, whose response function is shown in Fig. 2. The central frequency corresponds to a period of 45 days. The half-amplitude is at periods of 30 and 70 days. We have also tested the Lanczos filter (Duchan 1979), and the results are not sensitive to the different choice of filters. Although the ISO has seasonality in its amplitude and characteristics, intraseasonal variability at the equator is observed year-round, so we use all available data throughout the year.

For the long-term data and ARM data, an ISO composite is constructed using linear regression with respect to an ISO index. In this study, we use the 30–70-day filtered CMAP precipitation at a box within 5°N – 5°S , 145° – 150°E (surrounding Manus Island) as our ISO index. The confidence level of linear correlation is estimated following Oort and Yienger (1996). Figure 3a shows the lag regression between the ISO index and the CMAP precipitation for 23 yr (1979–2001) of data. As has been shown by many previous observations (e.g., Weickmann et al. 1985; Lau and Chan 1985; Rui and Wang 1990; Hendon and Salby 1994), the ISO consists of a precipitation anomaly that generally forms in the western Indian Ocean, amplifies to its first maximum in the eastern Indian Ocean, weakens over the Maritime

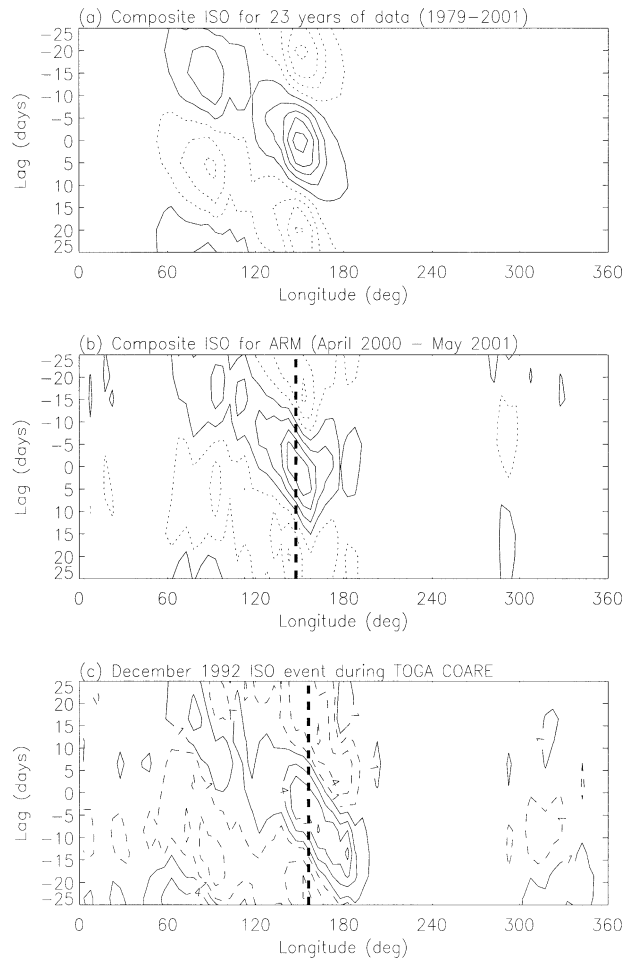


FIG. 3. (a) Lag regression between the 30–70-day CMAP precipitation anomaly and itself at 0° , 147°E for 23 yr (1979–2001) of data. (b) Lag regression between the 30–70-day CMAP precipitation anomaly and itself at 0° , 147°E for the ARM period (Apr 2000–May 2001). The thick dashed line is the longitude of Manus Island. (c) The 30–70-day CMAP precipitation anomaly during TOGA COARE. The thick dashed line is the longitude of IFA.

Continent, then reamplifies to a second maximum in the western Pacific before decaying near the date line. Its propagation speed is about 5 m s^{-1} in the eastern Indian Ocean and western Pacific. The composite for the ARM

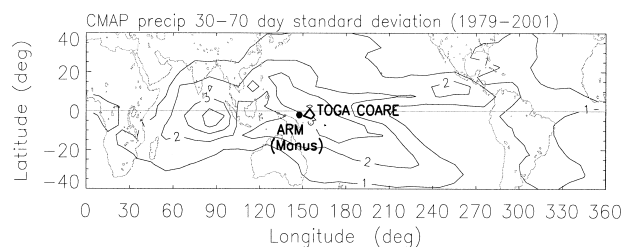


FIG. 4. Std dev of the 30–70-day bandpass-filtered anomaly of the CMAP precipitation from 1979 to 1999. The unit is mm day^{-1} . The black dot is ARM Manus site. The thick solid polygon is the IFA during TOGA COARE.

period (Fig. 3b) looks similar to the long-term composite (Fig. 3a). In particular, at the measurement longitude, the composite ISO propagates eastward with the typical phase speed of 5 m s^{-1} .

For the TOGA COARE data, we focus on the December 1992 ISO event (Fig. 3c). This is a strong ISO event with its amplitude at the TOGA COARE location larger than twice the standard deviation of the 23-yr data (Fig. 4). It moves eastward with a phase speed of 5 m s^{-1} , which is similar to the phase speed of the 23-yr composite (Fig. 3a). The maximum of the 30–70-day bandpass-filtered precipitation anomaly at the TOGA COARE IFA occurs on 21 December 1992.

4. Results

a. Intraseasonal variation of clouds and atmospheric properties

The variation of satellite-estimated total cloud during the composite ISO life cycle for ARM data is shown in Fig. 5. During precipitation, total cloud fraction increases due to the strong increase of high cloud fraction (Fig. 5a). Both middle and low cloud fraction appear to decrease, although this is likely an artifact of screening by high clouds. The averaged cloud-top height therefore increases (Fig. 5b). The cloud optical depth also increases because the high cloud becomes optically thicker (Fig. 5c). Figure 6 shows the associated variation of atmospheric properties as seen in sounding data. The vertically averaged temperature (Fig. 6a) leads precipitation by 5 days, while the vertically averaged water vapor mixing ratio (Fig. 6b) is exactly in phase with precipitation. The TOGA COARE cloud and sounding data show similar results as the ARM data (not shown).

b. Atmosphere radiation budget

The column-integrated diabatic heating can be written as (e.g., Yanai and Johnson 1993)

$$\begin{aligned} \langle Q_1 \rangle &= \langle Q_{\text{conv}} \rangle + \langle Q_R \rangle \\ &= LP + S + \langle Q_R \rangle, \end{aligned} \quad (1)$$

where

$$\langle \rangle = \int_{p_t}^{p_s} dp$$

is the integration from the tropopause pressure p_t to the surface pressure p_s . Here, Q_1 is the diabatic heating, Q_{conv} the convective heating, and Q_R the radiative heating; L the latent heat of vaporization, P the surface precipitation, and S the surface sensible heat flux. In the Tropics, S is generally much smaller than LP , and the column-integrated convective heating $\langle Q_{\text{conv}} \rangle \approx LP$.

Figure 7 shows the anomalous LP' and $\langle Q_R \rangle'$ during the composite ISO life cycle for 14 months of ARM data. Note that $\langle Q_R \rangle'$ slightly lags after LP' (by less than

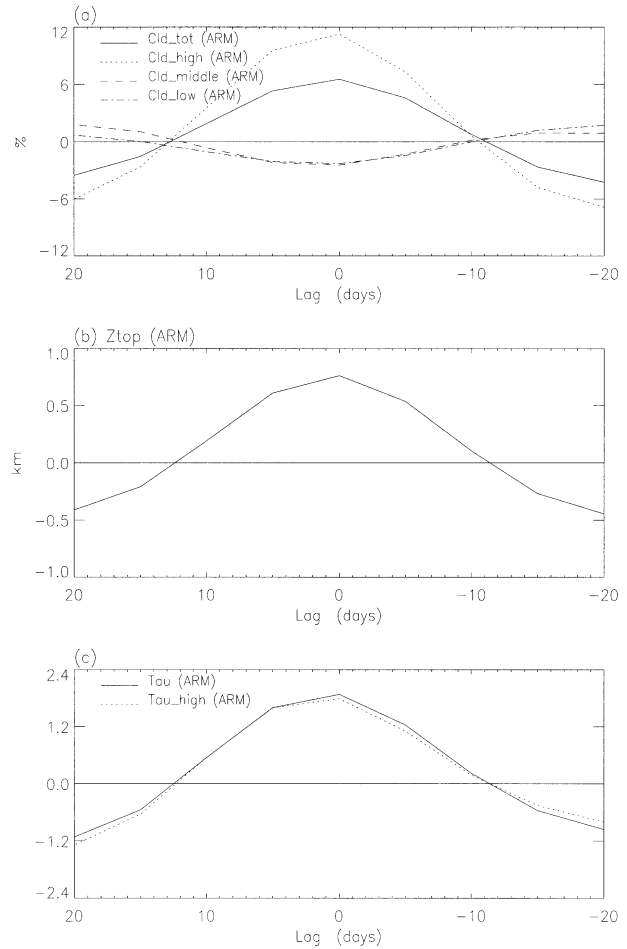


FIG. 5. Variation during the composite ISO life cycle for ARM data for (a) total cloud amount (solid line), high cloud amount (dotted line), middle cloud amount (dashed line), low cloud amount (dash-dotted line), (b) averaged cloud-top height, and (c) averaged cloud optical depth (solid line) and high cloud optical depth (dotted line). The abscissa is the time lag with respect to the time of maximum precipitation. The time evolution is from right to left, showing the local evolution as the eastward-moving intraseasonal oscillation passes the measurement longitude.

5 days), and its amplitude is 11% of that of LP' . Figure 8 is the same as Fig. 7 except for the December 1992 ISO event during TOGA COARE. Again $\langle Q_R \rangle'$ from TOA and surface flux measurements slightly lags after LP' by 1–2 days, and its amplitude is 16% of that of LP' , which is larger than the ARM result. The reason that it is larger may be that it is for one ISO event, while the ARM result is for the composite of many ISOs. The estimate of $\langle Q_R \rangle'$ derived from sounding array budgets has a much larger amplitude, 25% of that of LP' . The residual method for deriving $\langle Q_R \rangle'$ from sounding array budgets is limited by the errors in all other terms of the column-integrated moist static energy budget, such as the measurements of upper-air wind, temperature and humidity, and calculation of their gradients, plus errors in measurements of surface latent and sen-

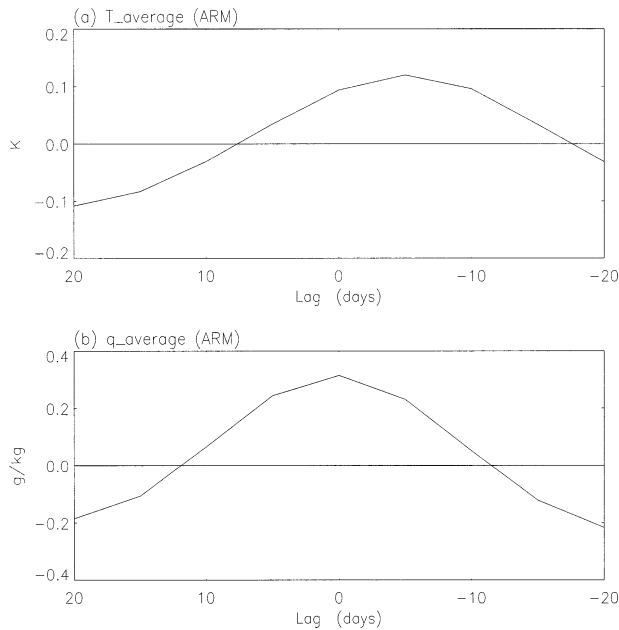


FIG. 6. As in Fig. 5 except for (a) vertically averaged temperature and (b) vertically averaged water vapor mixing ratio.

sible heat fluxes (Zhang and Lin 1997). Mapes et al. (2003) estimated that the random sampling error of IFA budget-derived $\langle Q_R \rangle$ is about 10 W m^{-2} for monthly mean, and 20 W m^{-2} for 5-day mean, which is close to its amplitude of the ISO variation (see Fig. 8b). Therefore, the budget-derived estimate is not accurate enough to pose a significant inconsistency with the 10%–15% values based on TOA and surface radiative flux data from ARM and COARE.

The $\langle Q_R \rangle'$ anomaly is dominated by the LW component as seen in Fig. 9. The dominant terms in the LW budget are shown in Fig. 10 for ARM and TOGA COARE data, with similar results. The dominant term is the TOA OLR (dotted line in Fig. 10), which slightly lags after the precipitation. Because the clear-sky OLR anomaly is small (Fig. 11), this reduced emission is caused primarily by increased high cloud amount (Figs. 5a,b), with a lesser contribution by increased atmospheric water vapor (Fig. 6b) during precipitation. The fact that clear-sky OLR decreases in the active phase (Fig. 11) indicates that the increased water vapor (Fig. 6b) is more important than the increased temperature (Fig. 6c). The “clear-sky greenhouse trapping” [defined by Raval and Ramanathan (1989) as the difference between the clear-sky OLR and the surface upwelling LW flux] increases by about 2 W m^{-2} (Fig. 11) per standard deviation of precipitation (110 W m^{-2}).

The surface downwelling LW flux (dashed line in Fig. 10) also shows an appreciable anomaly, out of phase with the precipitation, when increased clouds emit radiation from their bases down to the surface. The surface upwelling LW flux (dash-dotted line in Fig. 10) shows a small anomaly caused by the SST variation, which

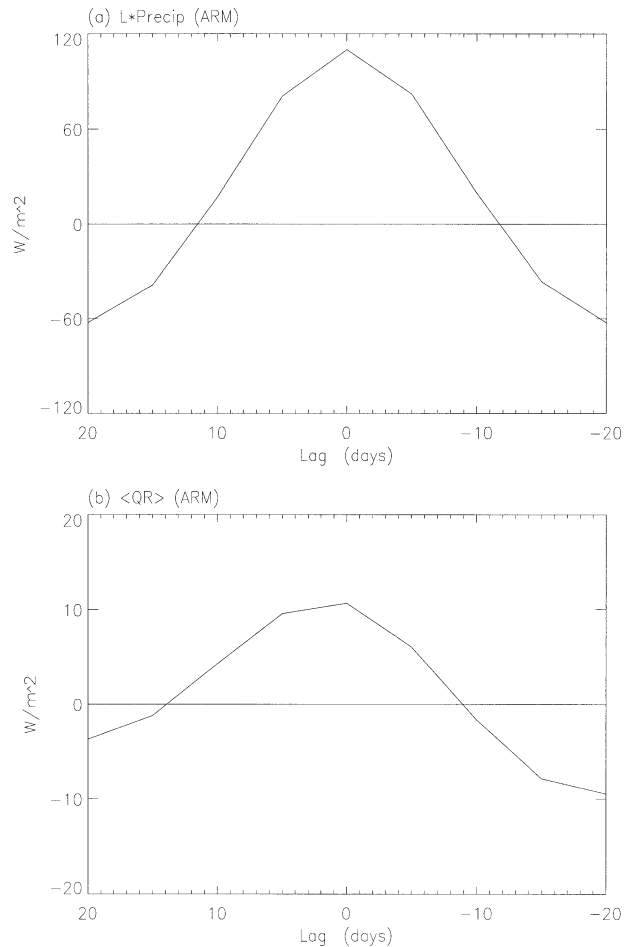


FIG. 7. As in Fig. 5 except for (a) LP' and (b) $\langle Q_R \rangle'$.

leads the precipitation by a quarter cycle (e.g., Zhang 1996; Hendon and Glick 1997). Because the surface downwelling LW flux anomaly cools the atmosphere column at the time of maximum precipitation, the LW atmospheric heating anomaly is always smaller than the OLR anomaly. Therefore, the OLR anomaly provides an upper limit for the LW heating anomaly and, in turn, for the total $\langle Q_R \rangle'$ anomaly because the SW heating anomaly is also slight cooling during the time of maximum precipitation. This makes it very convenient to estimate the upper limit (about 20% too large, based on these results) of $\langle Q_R \rangle'$ anomaly using the existing long-term OLR data from ERBE and AVHRR.

The SW component is smaller, contributing a slight cooling at the time of maximum precipitation, when there is increased high cloud amount (Fig. 5). Radiative transfer calculation showed that high clouds reduce the atmospheric shortwave absorption (Chen et al. 2000), although some uncertainties exist for the SW models in general (e.g., Cess et al. 1995, 1996). Our observational data cannot separate the cloud effect from the clear-sky effect because we do not have the clear-sky fluxes at the surface, which are very difficult to isolate even for

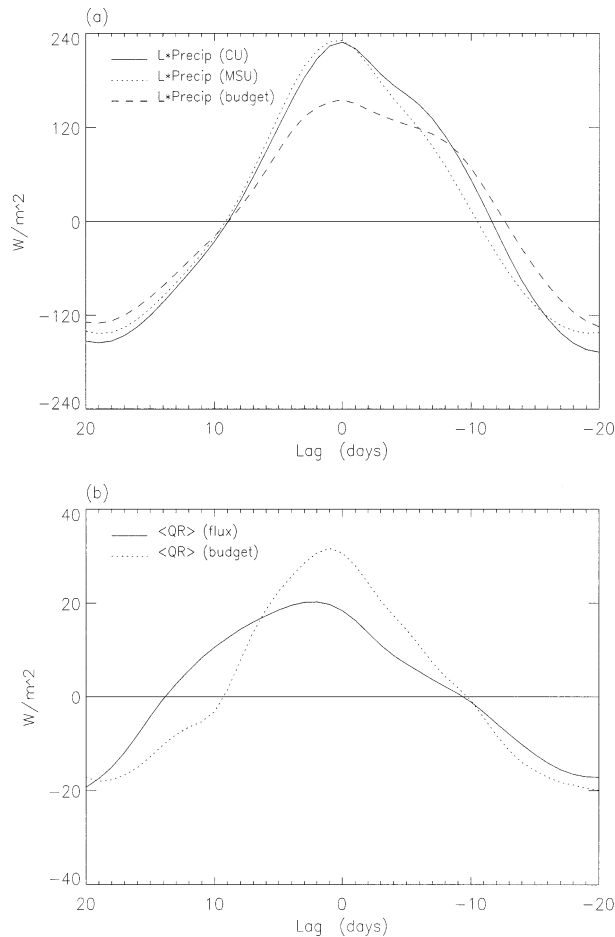


FIG. 8. As in Fig. 7 except for the Dec 1992 ISO event during TOGA COARE. (a) Three different precipitation estimates are plotted including SSM/I VIS-IR (solid line), MSU (dotted line), and that derived from sounding array budget (dashed line). (b) Two different radiative heating estimates are plotted including collocated satellite-surface flux measurement (solid line) and sounding array budget derived (dotted line).

the seasonal mean (e.g., Waliser et al. 1996; Chou and Zhao 1997), let alone at the intraseasonal time scale.

Figure 12 shows regressions against filtered CMAP of (Fig. 12a) the precipitation anomaly and (Fig. 12b) the OLR anomalies from ERBE (solid line) and AVHRR (dashed line) during the composite ISO life cycle at 0° , 155°E for 1985–89. The different precipitation datasets have some difference, with CMAP and GPI larger than MSU. The ERBE and AVHRR OLR data are remarkably consistent. The OLR anomaly is about 13% of the LP' anomaly when using CMAP or GPI precipitation, and 15% when using MSU precipitation. This upper limit of 15% for the relative $\langle Q_R \rangle'$ anomaly agrees with the ARM and TOGA COARE results (Figs. 7, 8).

Figure 13 shows the magnitudes of intraseasonal variations regressed against filtered CMAP at each longitude along the equator. Again, precipitation estimates by CMAP and GPI are systematically larger than MSU,

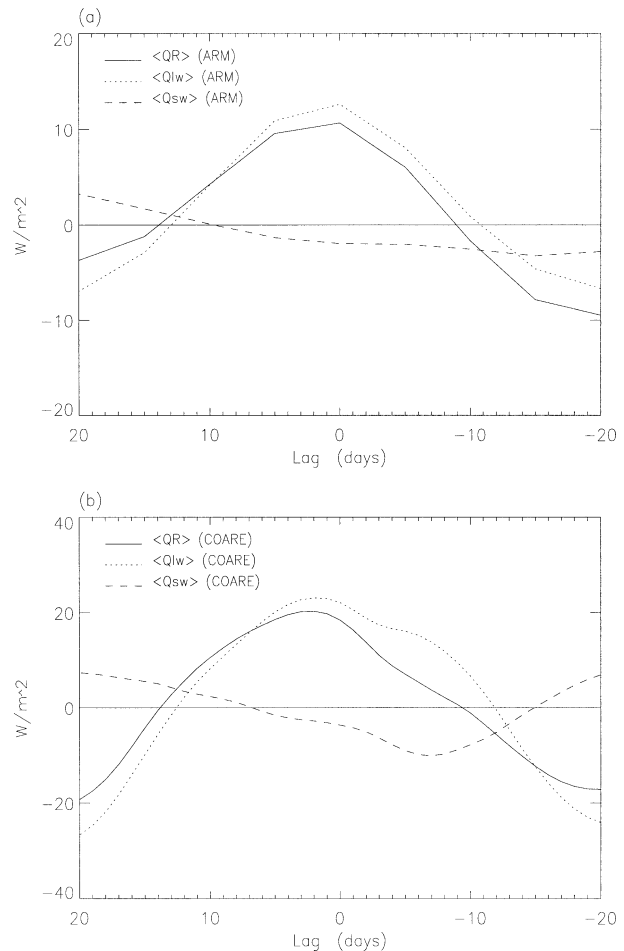


FIG. 9. As in Fig. 5 except for $\langle Q_R \rangle'$ (solid), $\langle Q_{LW} \rangle'$ (dotted), and $\langle Q_{sw} \rangle'$ (dashed) for (a) the composite ISO life cycle for ARM and (b) the Dec 1992 ISO event during TOGA COARE.

but the ERBE and AVHRR OLR data are quite consistent. In the Indo-Pacific warm pool region (80°E – 180°), the ratio between OLR' and LP' is less than 15% when using CMAP or GPI precipitation, and slightly larger than 15% when using MSU precipitation, which is consistent with 10%–15% from shorter-term single-longitude results from ARM and TOGA COARE.

In summary, all the different datasets consistently show that on intraseasonal time scales, column-integrated radiative heating lags the column-integrated convective heating by less than 5 days, and in the warm pool region it enhances the convective heating by about 10%–15%. To put this in perspective, recall that based on the vertical structure assumption of Yu et al. (1998), Lee et al. (2001) estimated that in order for the tropical atmosphere to reach radiative-convective instability, the enhancement factor of radiative heating needs to be larger than 20%.

It is interesting to note in Fig. 13 that the ratio between the OLR anomaly and LP' is much larger (over 20%) in the western Indian Ocean, which is the for-

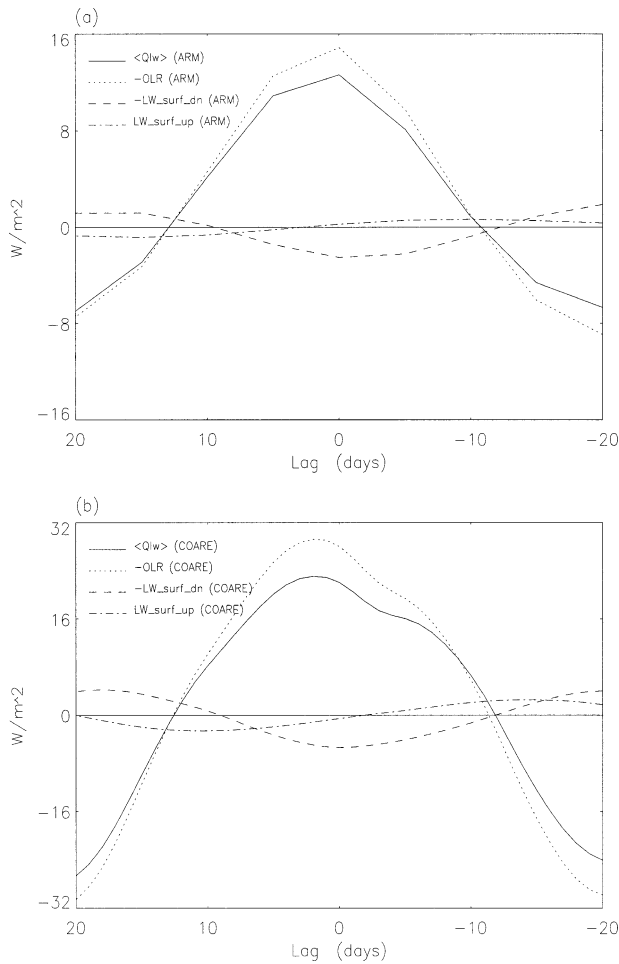


FIG. 10. As in Fig. 9 except for the LW budget terms, including $\langle Q_{LW} \rangle$ (solid), TOA upwelling LW flux (dotted), surface downwelling LW flux (dashed), and surface upwelling LW flux (dash-dotted).

mation region for the ISO (e.g., Rui and Wang 1990; Hendon and Salby 1994). This suggests that radiative-convective instability may play a role in the formation of the ISO, as proposed by Raymond (2001). Scatterplots of precipitation versus OLR anomalies in this region (not shown) indicate that OLR has a large intra-seasonal oscillation, while precipitation only has a very small oscillation. Although not associated with precipitation, cloud radiative effects may still “pump” the water vapor into the cloudy atmospheric column and premoisten it for deep convection, as demonstrated by Sherwood (1999) using a simple model.

c. TOA radiation budget

The TOA radiation budget is the energy input to the whole column (atmosphere plus ocean). Figure 14 shows that at TOA there is a substantial net radiative cooling during precipitation, about 10% of LP' (cf. Figs. 7a, 8a) for both the ARM sample (Fig. 14a) and the stronger COARE case study (Fig. 14b). The dominant

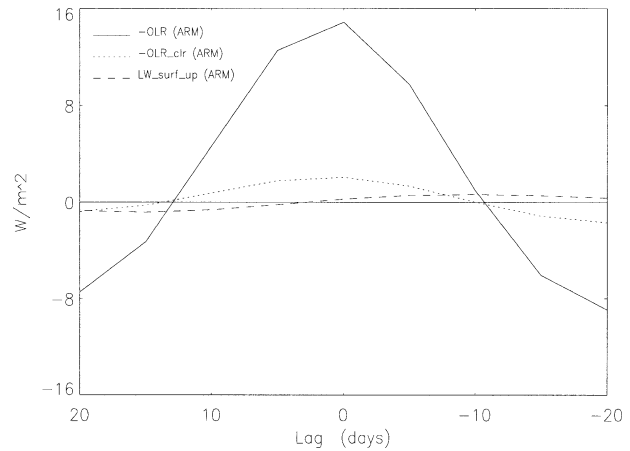


FIG. 11. As in Fig. 5 except for the TOA upwelling LW flux for all sky (solid) and clear sky (dotted), and the surface upwelling LW flux (dashed).

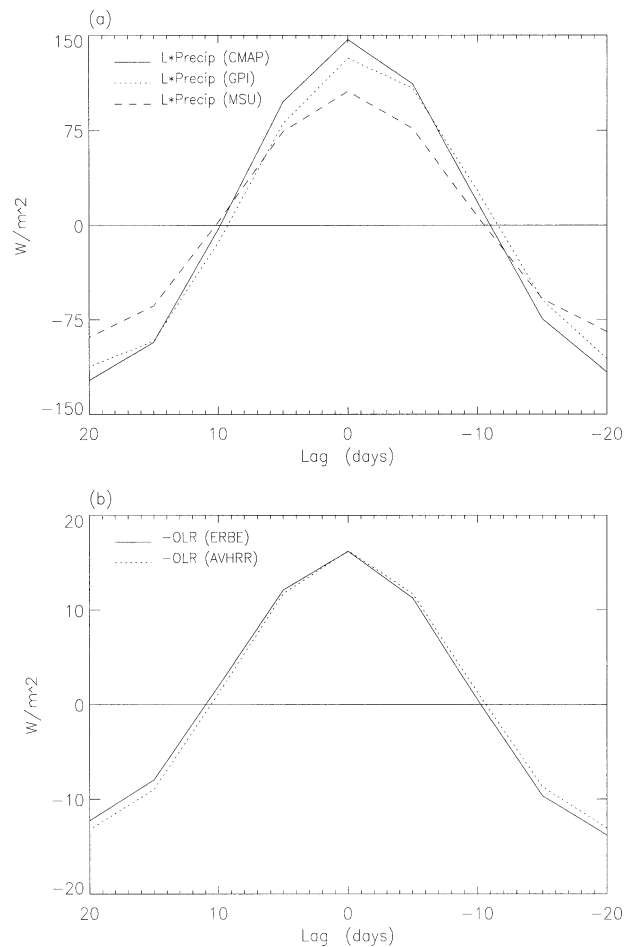


FIG. 12. Variation of (a) precipitation and (b) OLR during the composite ISO life cycle for 5 yr (1985–89) at 0° , 155°E . (a) Three different precipitation data are plotted, including CMAP (solid), GPI (dotted), and MSU (dashed). (b) Two different OLR data are plotted, including ERBE (solid) and AVHRR (dotted).

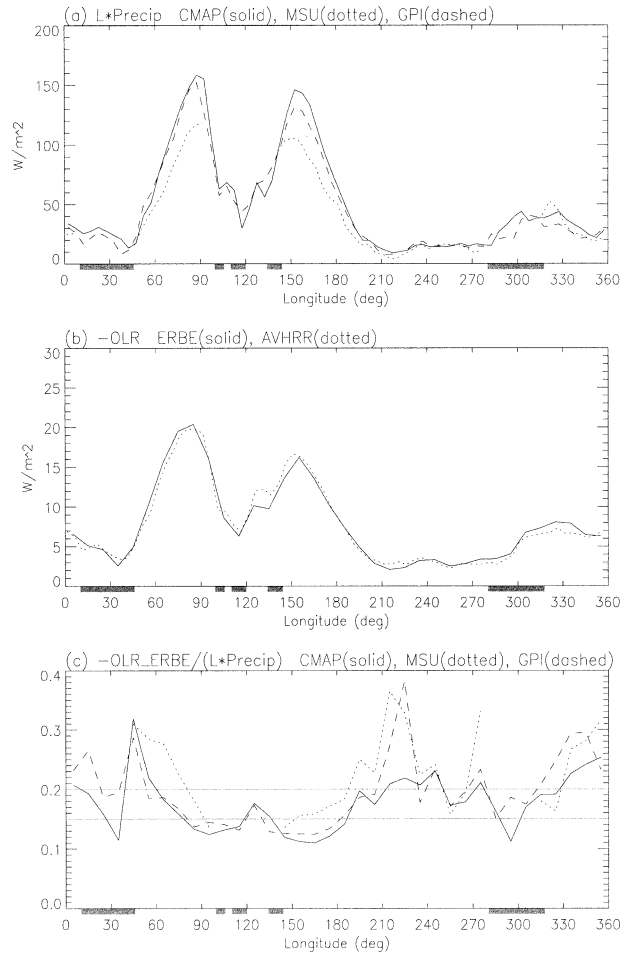


FIG. 13. Anomaly of (a) precipitation and (b) OLR at the time of maximum precipitation during the composite ISO life cycle for 5 yr (1985–89) along the equator. (a) Three different precipitation data are plotted, including CMAP (solid), GPI (dotted), and MSU (dashed). (b) Two different OLR data are plotted, including ERBE (solid) and AVHRR (dotted). (c) The ratio between the ERBE OLR anomaly and the three different precipitation data are plotted. The gray bars under (a)–(c) represent the continents along the equator.

effects is SW reflection by clouds, with only partial (~70%) cancellation by LW cloud effects (Fig. 15). This imperfect cancellation at intraseasonal time scales is in contrast with the near cancellation between SW and LW CRF at the seasonal time scale (e.g., Ramanathan et al. 1989; Harrison et al. 1990; Cess et al. 2001). Hartmann et al. (2001) and Cess et al. (2001) have shown that individual cloud types can have strongly positive or negative net CRF, with optically thin high clouds (cirrus) having positive net CRF, and optically thick high clouds and all middle and low clouds having negative net CRF (see Fig. 5 of Hartmann et al. 2001). The climatological near-zero net CRF is a balance between cirrus clouds and all other clouds (mainly optically thick high clouds in the western Pacific). However, large seasonal-mean negative net CRF has been observed in the Asian monsoon region (Rajeevan and Sri-

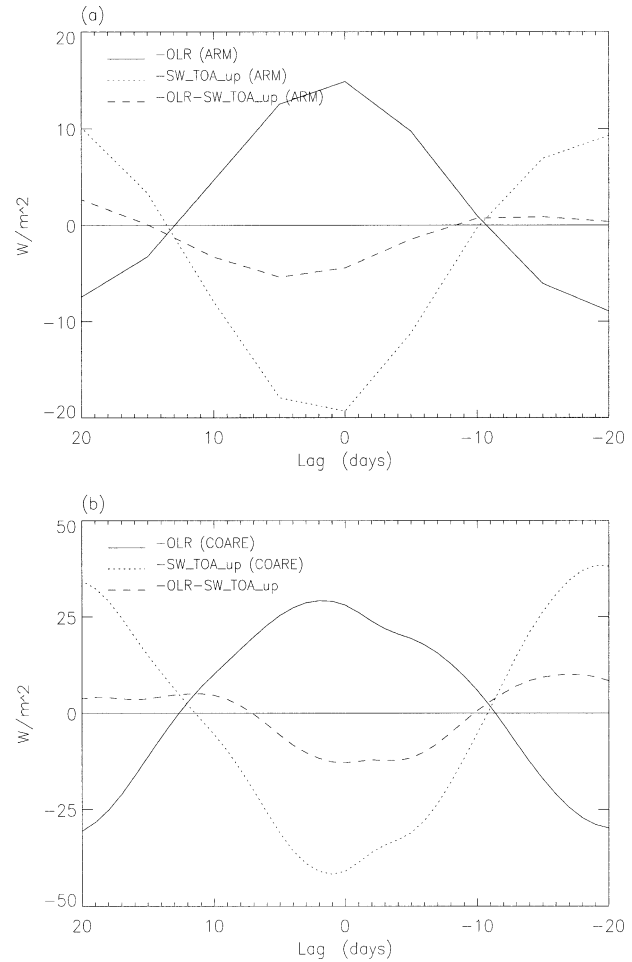


FIG. 14. As in Fig. 9 except for the TOA budget terms, including OLR (solid), TOA upwelling SW flux (dotted), and their sum (dashed).

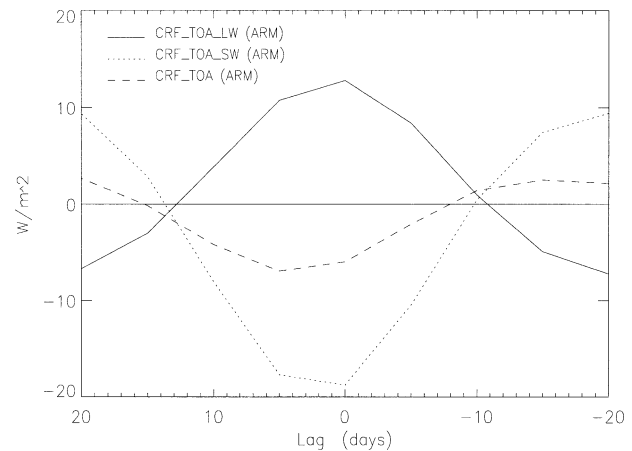


FIG. 15. As in Fig. 5 except for the TOA LW CRF (solid), TOA SW CRF (dotted), and TOA net CRF (dashed).

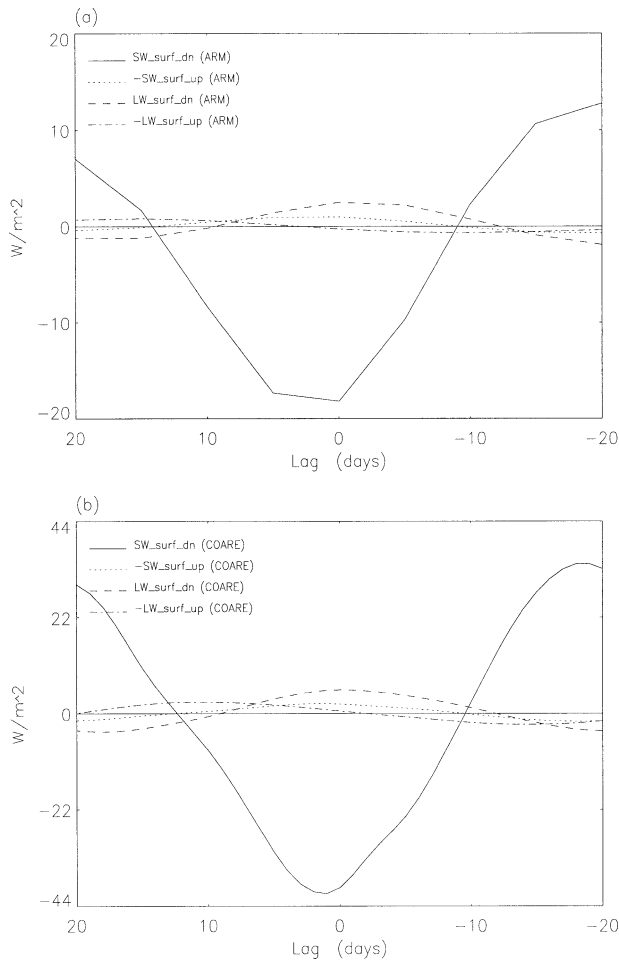


FIG. 16. As in Fig. 9 except for the surface budget terms, including surface downwelling SW flux (solid), surface upwelling SW flux (dotted), surface downwelling LW flux (dashed), and surface upwelling LW flux (dash-dotted).

nivasan 2000), associated with abundant optically thick high clouds in that region, and in the western Pacific warm pool during the strong 1998 El Niño (Cess et al. 2001), associated with an abundance of optically thick middle-level clouds. The large negative net CRF in the intraseasonal oscillation is associated with increased optically thick high clouds in the rainy areas, as shown in Fig. 5.

d. Surface radiation budget

The surface radiation budget is the energy input to the ocean. Figure 16 shows that the surface radiation budget is dominated by the downwelling SW flux anomaly. Shinoda et al. (1998, 1999) have shown that this downwelling SW flux anomaly plays an important role in the variation of the ocean mixed layer heat budget during the ISO.

ISO active-phase radiation budget

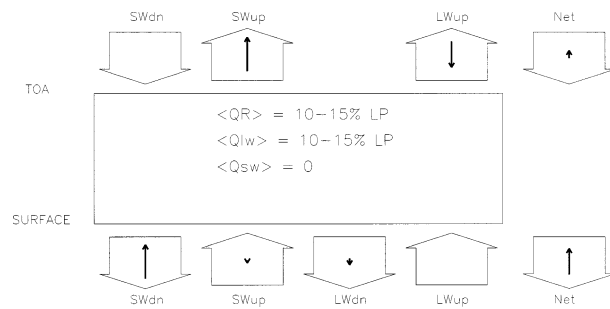


FIG. 17. Schematic illustration of the radiation budget at the time of maximum intraseasonal precipitation anomalies. The bulk arrows indicate the direction of the time-mean flux terms. The thin arrows indicate the anomalies of the corresponding flux terms, with its direction representing the sign of the anomaly, and its length representing the magnitude of the anomaly.

5. Summary

Intraseasonal variations of the atmospheric radiation budget have been estimated with collocated TOA and surface radiative flux measurements during ARM and TOGA COARE experiments, supplemented by long-term TOA flux measurement from ERBE and AVHRR. Results for a strong, classic ISO event in TOGA COARE are matched by composite time-filtered intraseasonal variability, indicating their generality. The major conclusions of this study are schematically summarized in Fig. 17. The conclusions may be divided into two categories: the atmospheric radiation budget and the TOA radiation budget.

For the atmospheric radiation budget, all the different datasets consistently show that column-integrated radiative heating lags the column-integrated convective heating by less than 5 days, and enhances the convective heating by about 10%–15%. This falls short of the 20% enhancement Lee et al. (2001) estimate as necessary for the atmosphere to reach radiative–convective instability, based on the assumptions set and results of Yu et al. (1998). There is some evidence that the enhancement factor is much larger (over 20%) in the western Indian Ocean, which is the formation region for the ISO, but this estimate reflects an especially uncertain ratio between small precipitation and OLR anomalies.

The atmospheric radiative heating during the convectively active phase is primarily in the longwave, as clouds and (slightly) water vapor reduce TOA outgoing longwave radiation (OLR). Surface downwelling longwave radiation and atmospheric shortwave absorption both provide slight cooling.

In the TOA radiation budget of the ISO, shortwave cloud forcing during the convectively active phase is about 30% larger than the opposite-signed longwave cloud forcing, indicating a net radiative energy sink to the ocean–atmosphere column. This result stands in con-

trast with the near cancellation between these two terms at the seasonal time scale.

Acknowledgments. Helpful discussions with Dave Randall, Dave Raymond, Chris Bretherton, and Adam Sobel are gratefully acknowledged, along with helpful reviews of the original manuscript by Adam Sobel, George Kiladis, and an anonymous reviewer. The GMS data were provided by Pat Minnis and Michele Nordeen, while the CAVE data were provided by Tom Charlock and Dave Rutan. Dave Rutan, Chuk Long, and Tom Stoffel generously provided detailed information on the quality of ARM data. ARM data are made available through the U.S. Department of Energy as part of the Atmospheric Radiation Measurement Program. This work was supported by the National Science Foundation Grants ATM-0097116, ATM-0073206, and ATM-0112715.

REFERENCES

- Barkstrom, B. R., and G. L. Smith, 1986: The Earth Radiation Budget Experiment: Science and implementation. *Rev. Geophys.*, **24**, 379–390.
- Bergman, J. W., H. H. Hendon, and K. M. Weickmann, 2001: Intraseasonal air–sea interactions at the onset of El Niño. *J. Climate*, **14**, 1702–1719.
- Blade, I., and D. L. Hartmann, 1993: Tropical intraseasonal oscillations in a simple nonlinear model. *J. Atmos. Sci.*, **50**, 2922–2939.
- Burks, J. E., 1998: Radiative fluxes and heating rates during TOGA COARE over the intensive flux array. M.S. thesis, Dept. of Meteorology, University of Utah, 85 pp.
- Cess, R. D., 1976: Climate change: An appraisal of atmospheric feedback mechanisms employing zonal climatology. *J. Atmos. Sci.*, **33**, 1831–1843.
- , and Coauthors, 1995: Absorption of solar radiation by clouds: Observations versus models. *Science*, **267**, 496–499.
- , M. H. Zhang, Y. Zhou, X. Jing, and V. Dvortsov, 1996: Absorption of solar radiation by clouds: Interpretations of satellite, surface, and aircraft measurements. *J. Geophys. Res.*, **101**, 23 299–23 309.
- , B. A. Wielicki, D. F. Young, X.-L. Zhou, and Y. Nikitenko, 2001: The influence of the 1998 El Niño upon cloud-radiative forcing over the Pacific warm pool. *J. Climate*, **14**, 2129–2137.
- Chen, T., W. B. Rossow, and Y. Zhang, 2000: Radiative effects of cloud-type variations. *J. Climate*, **13**, 264–286.
- Chou, M.-D., and W. Zhao, 1997: Estimation and model validation of surface solar radiation and cloud radiative forcing using TOGA COARE measurements. *J. Climate*, **10**, 610–620.
- , —, and S. H. Chou, 1998: Radiation budgets and cloud radiative forcing in the Pacific warm pool during TOGA COARE. *J. Geophys. Res.*, **103**, 16 967–16 977.
- Ciesielski, P. E., R. H. Johnson, and J. Wang, 2002: Impacts of humidity-corrected sonde data on TOGA COARE analyses. Preprints, *25th Conf. on Hurricanes and Tropical Meteorology*, San Diego, CA, Amer. Meteor. Soc., CD-ROM, 4B.1.
- Collins, W. D., F. P. J. Valero, P. J. Flatau, D. Lubin, H. Grassl, and P. Pilewskie, 1996: Radiative effects of convection in the tropical Pacific. *J. Geophys. Res.*, **101**, 14 999–15 012.
- Curry, J. A., C. A. Clayson, W. B. Rossow, R. Reeder, Y.-C. Zhang, P. J. Webster, G. Liu, and R. S. Sheu, 1999: High-resolution satellite-derived dataset of the surface fluxes of heat, freshwater, and momentum for the TOGA COARE IOP. *Bull. Amer. Meteor. Soc.*, **80**, 2059–2080.
- Doelling, D. R., P. Minnis, R. Palikonda, and D. A. Spangenberg, 1998: Validation of broadband fluxes derived from GMS during TOGA/COARE. *Proc. CLIVAR/GEWEX COARE98 Conf.*, Boulder, CO, National Institute of Standards and Technology, WCRP-107, WMO Tech. Doc. 940, 241–242.
- Duchan, C. E., 1979: Lanczos filtering in one and two dimensions. *J. Appl. Meteor.*, **18**, 1016–1022.
- Emanuel, K. A., 1987: An air–sea interaction model of intraseasonal oscillation in the Tropics. *J. Atmos. Sci.*, **44**, 2324–2340.
- Harrison, E. F., P. Minnis, B. R. Barkstrom, V. Ramanathan, R. D. Cess, and G. G. Gibson, 1990: Seasonal variation of cloud radiative forcing derived from the Earth Radiation Budget Experiment. *J. Geophys. Res.*, **95**, 18 687–18 703.
- Hartmann, D. L., L. A. Moy, and Q. Fu, 2001: Tropical convection and the energy balance at the top of the atmosphere. *J. Climate*, **14**, 4495–4511.
- Hayashi, Y., and D. G. Golder, 1986: Tropical intraseasonal oscillations appearing in a GFDL general circulation model and FGGE data. Part I: Phase propagation. *J. Atmos. Sci.*, **43**, 3058–3067.
- , and A. Sumi, 1986: The 30–40 day oscillation simulated in an “aqua planet” model. *J. Meteor. Soc. Japan*, **64**, 451–466.
- , and D. G. Golder, 1988: Tropical intraseasonal oscillations appearing in a GFDL general circulation model and FGGE data. Part II: Structure. *J. Atmos. Sci.*, **45**, 3017–3033.
- , and —, 1997: United mechanisms for the generation of low- and high-frequency tropical waves. Part I: Control experiments with moist convective adjustments. *J. Atmos. Sci.*, **54**, 1262–1276.
- Hendon, H. H., and B. Liebmann, 1990: A composite study of onset of the Australia monsoon. *J. Atmos. Sci.*, **47**, 2227–2240.
- , and M. L. Salby, 1994: The life cycle of the Madden–Julian oscillation. *J. Atmos. Sci.*, **51**, 2225–2237.
- , and J. D. Glick, 1997: Intraseasonal air–sea interaction in the tropical Indian and Pacific Oceans. *J. Climate*, **10**, 647–661.
- Higgins, R. W., and K. C. Mo, 1997: Persistent North Pacific circulation anomalies and the tropical intraseasonal oscillation. *J. Climate*, **10**, 223–244.
- Janowiak, J. E., and P. A. Arkin, 1991: Rainfall variations in the Tropics during 1986–1989, as estimated from observations of cloud-top temperatures. *J. Geophys. Res.*, **96** (Suppl.), 3359–3373.
- Johnson, R. H., and P. E. Ciesielski, 2000: Rainfall and radiative heating rates from TOGA COARE atmospheric budgets. *J. Atmos. Sci.*, **57**, 1497–1514.
- Kessler, W. S., M. J. McPhaden, and K. M. Weickmann, 1995: Forcing of intraseasonal Kelvin waves in the equatorial Pacific. *J. Geophys. Res.*, **100**, 10 613–10 631.
- Krishnamurti, T.-N., P. K. Jayakumar, J. Sheng, N. Surgi, and A. Kuma, 1985: Divergent circulations on the 30 to 50 day time-scale. *J. Atmos. Sci.*, **42**, 364–375.
- Krueger, S. K., and J. E. Burks, 1998: Radiative fluxes and heating rates during TOGA COARE over the intensive flux array. *Proc. CLIVAR/GEWEX COARE98 Conf.*, Boulder, CO, National Institute of Standards and Technology, WCRP-107, WMO Tech. Doc. 940, 239–240.
- Lau, K. M., and P. H. Chan, 1985: Aspects of the 40–50-day oscillation during the northern winter as inferred from outgoing long-wave radiation. *Mon. Wea. Rev.*, **113**, 1889–1909.
- , and L. Peng, 1987: Origin of low-frequency (intraseasonal) oscillations in the tropical atmosphere. *J. Atmos. Sci.*, **44**, 950–972.
- Lau, N. C., I. M. Held, and J. D. Neelin, 1988: The Madden–Julian oscillation in an idealized general circulation model. *J. Atmos. Sci.*, **45**, 3810–3832.
- Lee, M.-I., I.-S. Kang, J.-K. Kim, and B. E. Mapes, 2001: Influence of cloud–radiation interaction on simulating tropical intraseasonal oscillation with an atmospheric general circulation model. *J. Geophys. Res.*, **106**, 14 219–14 233.
- Liebmann, B., and C. A. Smith, 1996: Description of a complete

- (interpolated) outgoing longwave radiation dataset. *Bull. Amer. Meteor. Soc.*, **77**, 1275–1277.
- , H. H. Hendon, and J. D. Glick, 1994: The relationship between tropical cyclones of the western Pacific and Indian Oceans and the Madden-Julian oscillation. *J. Meteor. Soc. Japan*, **72**, 401–411.
- Long, C. N., and T. P. Ackerman, 1995: Surface measurements of solar irradiance: A study of the spatial correlation between simultaneous measurements at separated sites. *J. Appl. Meteor.*, **34**, 1039–1046.
- Madden, R. A., and P. R. Julian, 1971: Detection of a 40–50 day oscillation in the zonal wind in the tropical Pacific. *J. Atmos. Sci.*, **28**, 702–708.
- , and —, 1972: Description of global-scale circulation cells in the Tropics with a 40–50 day period. *J. Atmos. Sci.*, **29**, 1109–1123.
- , and —, 1994: Observations of the 40–50-day tropical oscillation—A review. *Mon. Wea. Rev.*, **122**, 814–837.
- Mapes, B. E., P. E. Ciesielski, and R. H. Johnson, 2003: Sampling errors in rawinsonde-array budgets. *J. Atmos. Sci.*, **60**, 2697–2714.
- Mather, J. H., T. P. Ackerman, W. E. Clements, F. J. Barnes, M. D. Ivey, L. D. Hatfield, and R. M. Reynolds, 1998: An atmospheric radiation and cloud station in the tropical western Pacific. *Bull. Amer. Meteor. Soc.*, **79**, 627–642.
- Minnis, P., W. L. Smith Jr., D. P. Garber, J. K. Ayers, and D. R. Doelling, 1995: Cloud properties derived from GOES-7 for the spring 1994 ARM intensive observing period using version 1.0.0 of the ARM Satellite Data Analysis Program. NASA Rep. 1366, 59 pp.
- Murakami, M., 1979: Large-scale aspects of deep convective activity over the GATE area. *Mon. Wea. Rev.*, **107**, 994–1013.
- Murakami, T., and T. Nakazawa, 1985: Tropical 45 day oscillations during the 1979 Northern Hemisphere summer. *J. Atmos. Sci.*, **42**, 1107–1122.
- Neelin, J. D., I. M. Held, and K. H. Cook, 1987: Evaporation–wind feedback and low-frequency variability in the tropical atmosphere. *J. Atmos. Sci.*, **44**, 2341–2348.
- Oort, A. H., and J. J. Yienger, 1996: Observed long-term variability in the Hadley circulation and its connection to ENSO. *J. Climate*, **9**, 2751–2767.
- Rajeevan, M., and J. Srinivasan, 2000: Net cloud radiative forcing at the top of the atmosphere in the Asian monsoon region. *J. Climate*, **13**, 650–657.
- Ramanathan, V., R. D. Cess, E. F. Harrison, P. Minnis, B. R. Barkstrom, E. Ahmad, and D. Hartmann, 1989: Cloud-radiative forcing and climate: Results from the Earth Radiation Budget Experiment. *Science*, **243**, 57–63.
- Raval, A., and V. Ramanathan, 1989: Observational determination of the greenhouse effect. *Nature*, **342**, 758–762.
- Raymond, D. J., 2001: A new model of the Madden-Julian oscillation. *J. Atmos. Sci.*, **58**, 2807–2819.
- Reynolds, R. W., N. A. Rayner, T. M. Smith, D. C. Stokes, and W. Wang, 2002: An improved in situ and satellite SST analysis for climate. *J. Climate*, **15**, 1609–1625.
- Rossow, W. B., and L. C. Gardner, 1993: Cloud detection using satellite measurements of infrared and visible radiances for ISSCP. *J. Climate*, **6**, 1403–1420.
- Rui, H., and B. Wang, 1990: Development characteristics and dynamic structure of tropical intraseasonal convection anomalies. *J. Atmos. Sci.*, **47**, 357–379.
- Rutan, D. A., F. G. Rose, N. M. Smith and T. P. Charlock, 2001: Validation data set for CERES surface and atmospheric radiation budget (SARB). *WCRP/GEWEX Newsletter*, Vol. 11, No. 1, International GEWEX Project Office, 11–12.
- Salby, M. L., and H. H. Hendon, 1994: Intraseasonal behavior of clouds, temperature, and motion in the Tropics. *J. Atmos. Sci.*, **51**, 2207–2224.
- Sherwood, S. C., 1999: On moistening of the tropical troposphere by cirrus clouds. *J. Geophys. Res.*, **104**, 11 949–11 960.
- Shinoda, T., H. H. Hendon, and J. Glick, 1998: Intraseasonal variability of surface fluxes and sea surface temperature in the tropical western Pacific and Indian Oceans. *J. Climate*, **11**, 1685–1702.
- , —, and —, 1999: Intraseasonal surface fluxes in the tropical western Pacific and Indian Oceans from NCEP reanalyses. *Mon. Wea. Rev.*, **127**, 678–693.
- Slingo, J. M., and Coauthors, 1996: Intraseasonal oscillations in 15 atmospheric general circulation models: Results from an AMIP diagnostic subproject. *Climate Dyn.*, **12**, 325–357.
- Sobel, A. H., and H. Gildor, 2003: A simple time-dependent model of SST hot spots. *J. Climate*, **16**, 3978–3992.
- Spencer, R. W., 1993: Global oceanic precipitation from the MSU during 1979–91 and comparisons to other climatologies. *J. Climate*, **6**, 1301–1326.
- Takayabu, Y. N., T. Iguchi, M. Kachi, A. Shibata, and H. Kanzawa, 1999: Abrupt termination of the 1997–98 El Niño in response to a Madden-Julian oscillation. *Nature*, **402**, 279–282.
- Vonder Haar, T. H., and V. E. Suomi, 1969: Satellite observations of the earth's radiation budget. *Science*, **163**, 667–669.
- Waliser, D. E., W. D. Collins, and S. P. Anderson, 1996: An estimate of the surface shortwave cloud forcing over the western Pacific during TOGA COARE. *Geophys. Res. Lett.*, **23**, 519–522.
- Weickmann, K. M., G. R. Lussky, and J. E. Kutzbach, 1985: Intraseasonal (30–60 day) fluctuations of outgoing longwave radiation and 250 mb streamfunction during northern winter. *Mon. Wea. Rev.*, **113**, 941–961.
- Weller, R. A., and S. P. Anderson, 1996: Surface meteorology and air–sea fluxes in the western equatorial Pacific warm pool during the TOGA Coupled Ocean–Atmosphere Response Experiment. *J. Climate*, **9**, 1959–1992.
- Wheeler, M., and G. N. Kiladis, 1999: Convectively coupled equatorial waves: Analysis of clouds and temperature in the wave-number–frequency domain. *J. Atmos. Sci.*, **56**, 374–399.
- Wielicki, B. A., B. R. Barkstrom, E. F. Harrison, R. B. Lee III, G. L. Smith, and J. E. Cooper, 1996: Clouds and the Earth's Radiant Energy System (CERES): An Earth Observing System Experiment. *Bull. Amer. Meteor. Soc.*, **77**, 853–868.
- Xie, P., and P. A. Arkin, 1997: Global precipitation: A 17-year monthly analysis based on gauge observations, satellite estimates, and numerical model outputs. *Bull. Amer. Meteor. Soc.*, **78**, 2539–2558.
- Yanai, M., and R. H. Johnson, 1993: Impacts of cumulus convection on thermodynamic fields. *The Representation of Cumulus Convection in Numerical Models of the Atmosphere*, Meteor. Monogr., No. 46, Amer. Meteor. Soc., 39–62.
- , B. Chen, and W.-W. Tung, 2000: The Madden-Julian oscillation observed during the TOGA COARE IOP: Global view. *J. Atmos. Sci.*, **57**, 2374–2396.
- Yasunari, T., 1979: Cloudiness fluctuations associated with the Northern Hemisphere summer monsoon. *J. Meteor. Soc. Japan*, **57**, 227–242.
- Yu, J.-Y., C. Chou, and J. D. Neelin, 1998: Estimating the gross moist stability of the tropical atmosphere. *J. Atmos. Sci.*, **55**, 1354–1372.
- Zhang, C., 1996: Atmospheric intraseasonal variability at the surface in the tropical western Pacific Ocean. *J. Atmos. Sci.*, **53**, 739–758.
- Zhang, M. H., and J. L. Lin, 1997: Constrained variational analysis of sounding data based on column-integrated budgets of mass, heat, moisture, and momentum: Approach and application to ARM measurements. *J. Atmos. Sci.*, **54**, 1503–1524.